Superresolution Diffuse Optical Imaging by Localization of Fluorescence

Brian Z. Bentz, Dergan Lin, and Kevin J. Webb

Phys. Rev. Applied **10**, 034021 — Published 11 September 2018

DOI: 10.1103/PhysRevApplied.10.034021

Super-resolution diffuse optical imaging by localization of fluorescence

Brian Z. Bentz,[1,2] Dergan Lin,[2] and Kevin J. Webb[2,*]

[1] *Sandia National Laboratories, Albuquerque, New Mexico 87123, USA*

[2] *Purdue University, West Lafayette, Indiana 47907, USA*

Abstract

The multiple scattering of light presents major challenges in realizing useful *in vivo* imaging at tissue depths of more than about one millimeter where many answers to health questions lie. Visible through near-infrared photons can be readily and safely detected through centimeters of tissue, however limited information is available for image formation. One strategy for obtaining images is to model the photon transport, and a simple incoherent model is the diffusion equation approximation to the Boltzmann transport equation. Such an approach provides a prediction of the mean intensity of heavily scattered light and hence provides a forward model for optimization-based computational imaging. While diffuse optical imaging methods have received substantial attention, they remain restricted in terms of resolution because of the loss of high spatial frequency information that is associated with the multiple scattering of photons. Consequently, only relatively large inhomogeneities, such as tumors or organs in small animals, can be effectively resolved. Here, we introduce a super-resolution imaging approach based on point localization in a diffusion framework that enables over two orders of magnitude improvement in the spatial resolution of diffuse optical imaging. The method is demonstrated experimentally by localizing a fluorescent inhomogeneity in a highly scattering slab and characterizing the localization uncertainty. The approach allows imaging through centimeters of tissue with a resolution of tens of microns, thereby enabling cells or cell clusters to be resolved. More generally, this high-resolution imaging approach could be applied with any physical transport or wave model and hence to a broad class of physical problems. Paired with a suitable optical contrast mechanism, as can be realized with targeted fluorescent molecules or genetically-modified animals, super-resolution diffuse imaging should open new dimensions for *in vivo* applications.

---

[*] webb@purdue.edu

I. INTRODUCTION

The interaction of light with tissue has received intense study due to a myriad of applications in biomedical science [1–3]. Near the tissue surface, coherent methods are used to image with spatial resolutions at the diffraction limit [4]. However, in deep tissue where the propagation direction of light is randomized due to optical scattering, forming an image becomes a much greater challenge. Coherent imaging is still possible, for example, through feedback control of the amplitude and phase of the incident wavefront, which has allowed focusing of light to depths of about 1 mm in tissue [5]. Alternatively, the tissue can be characterized through measurement and inversion of a field transmission matrix, allowing image formation [6–8]. These types of coherent methods can achieve high resolution, however they are generally less effective as the amount of scatter increases, limiting their applications in deep ($>$ 1 cm) tissue. Coherent imaging through almost any amount of scatter is possible using speckle intensity correlations over object position [9, 10]. However, this method requires that the positional change of the object is known or can be estimated.

Deep tissue imaging is achievable with diffuse optical imaging (DOI), a computational imaging method where a model of light transport in scattering media allow extraction of images from incoherent light [2, 3, 11, 12]. For example, in diffuse optical tomography (DOT) [3, 13–15], three-dimensional images of the spatially-dependent optical properties are iteratively reconstructed from boundary measurements of highly scattered light. With the addition of fluorescent contrast agents, fluorescence diffuse optical tomography (FDOT) allows computational imaging of targeted biochemical pathways [16, 17]. FDOT has proven especially useful for *in vivo* small animal studies of, for example, targeted drugs [18] and misfolding of protein aggregates [19]. However, the low resolution of DOI methods such as FDOT compared to coherent methods [20] has restricted the applications.

Here, we present a method to circumvent previous DOI resolution limits. We use optical localization, where information about the location of the centroid of an inhomogeneity is extracted. We call the method super-resolution diffuse optical imaging (SRDOI). The case we consider is a small region embedded in a heavily scattering background that contains fluorophores. Multiple fluorescent regions could be similarly imaged at high resolution when the emission from each region is separable, for example, through sufficient spatial, temporal, or spectral separation, or a combination of these. The results indicate that by localizing many inhomogeneities individually within a highly scattering medium and combining the positions into a single image, high resolution DOI can be achieved. Previous studies have localized fluorescent inhomogeneities in deep tissue [21–24]. For example, boundary measurements of fluorescence emission have allowed extraction of the location of fluorescing tumors [23, 25]. In these studies, tumor masses were localized after injecting mice with fluorescent contrast agents that targeted specific cancer cells. However, the implications and limits for high resolution imaging have not been previously examined.

In Section II, the diffusion model for light propagation is described, and the spatial resolution that has been achieved by DOI in the literature is considered, as a comparison for SRDOI. In Section III, the fluorescent localization method is presented, including the derivation of the forward model and the optimization procedure. In Section IV, the performance of SRDOI is characterized with numerical simulation and experimental validation in a slab geometry. The SRDOI results demonstrate two orders of magnitude improvement in the spatial resolution compared to FDOT.

II. DIFFUSE OPTICAL IMAGING

Optical transport in tissue can be described by the radiative transfer equation, and under restrictions on scattering strength (weak), absorption (weak), and time (long compared to the scattering time), and with sufficient scatter, the diffusion approximation provides a simple model [3, 13]. In the frequency domain, the light source is modulated at angular frequency ω, i.e., we assume $\exp(-i\omega t)$ variation. For a fluorescence source in a locally homogeneous medium, the coupled diffusion equations can then be written in the form of wave equations as [17]

$$\nabla^2\phi_x(\mathbf{r}) + k_x^2\phi_x(\mathbf{r}) = -S_x(\mathbf{r},\omega) \tag{1}$$

$$\nabla^2\phi_m(\mathbf{r}) + k_m^2\phi_m(\mathbf{r}) = -\phi_x(\mathbf{r})S_f(\mathbf{r},\omega), \tag{2}$$

where $\mathbf{r}$ denotes position, ϕ (W/mm^2) is the photon flux density, the subscripts x and m, respectively, denote parameters at the fluorophore excitation and emission wavelengths, λ_x and λ_m, $k^2 = -\mu_a/D + i\omega/(Dv)$, where $D = 1/[3(\mu_s' + \mu_a)]$ (mm) is the diffusion coefficient, μ_s' is the reduced scattering coefficient, μ_a is the absorption coefficient, v is the speed of light within the medium, $S_x(\mathbf{r},\omega)$ is the excitation source, and $S_f(\mathbf{r},\omega)$ describes the fluorescence emission. In an infinite homogeneous space, the frequency domain diffusion equation (written as a lossy wave equation) Green's function is

$$g(\mathbf{r}', \mathbf{r}) = \frac{e^{ik|\mathbf{r}-\mathbf{r}'|}}{4\pi|\mathbf{r}-\mathbf{r}'|}, \tag{3}$$

where $\mathbf{r}'$ is the position of a point source and the complex wave number k is applied at λ_x or λ_m in (1) or (2) respectively.

Solutions to (1) and (2) are called diffuse photon density waves (DPDW's) [2, 26, 27]. Here, we refer to data formed through experimental detection of DPDW's as measurements. In Section III A, we derive a forward model using (1) and (2), which we treat as an estimate of the expected values of the measurements. In contrast, images recovered using an inversion method (an indirect imaging method that extracts desired parameters (e.g., $\mathbf{r}'$) from measurement data (e.g., ϕ) through inversion of a forward model) are referred to as reconstructed images. The resolution of a reconstructed image depends on the method used (see for example, [28, 29]). Of note, the treatment of the nonlinear nature of the inversion process and the use of constraints (or a prior model in a Bayesian sense) can be of substantial consequence.

Even without absorption, the DPDW wavenumber is complex, implying that there is always both propagation and attenuation at any spatial frequency [27]. The wavelength of DPDW's for typical tissue and modulation frequencies (10 MHz or so) is on the order of a few centimeters. Measurements are therefore usually made within distances less than about one wavelength from a source location, placing them in the near field in this sense. However, the attenuation of high spatial frequencies is still severe, causing a significant reduction in resolution with depth. Here, we define resolution as the full width at half max (FWHM) of the point spread function (PSF), where the PSF is the image of a point source located in the scattering medium. Equivalently, the resolution is the distance between two identical point sources such that their PSFs intersect at their FWHM.

The dependence of the resolution on depth is nonlinear and has been estimated using the FWHM of the propagation transfer function in a homogeneous infinite medium [27]. The resolution is unrelated to the diffraction limit because DPDW's have a complex wavenumber and are measured in the near field. The resolution depends primarily on μ_s', μ_a, and the distance from the source to detectors. Practically, however, the resolution depends on many other factors, including the measurement signal-to-noise ratio (SNR), the medium geometry, the source-detector diversity, the contrast between the inhomogeneity and the background, and the experimental setup. For the case of reconstructed images, the resolution will also depend on the computational method used for reconstruction.

As a comparison for the work presented here, Fig. 1 shows a plot of the resolutions achieved based on both measured data (without reconstruction of an image) and image reconstructions (though a computational imaging procedure). The red symbols are reconstructed image resolutions (without prior information), and the blue symbols are direct measurement resolutions. The blue curves are analytical resolution limits of direct measurements for μ_s' and μ_a typical of tissue, as calculated by Ripoll *et al.* [27]. From Fig. 1, we find that for optical properties similar to tissue and beyond a depth of about 1 cm, the reported reconstructed image resolution is typically about depth/2, as represented by the dashed black line.

The resolution in Fig. 1 can be improved with the incorporation of prior information that constrains the inverse problem. When combined with other imaging modalities, such as MRI [30, 31], the resolution can be improved to that of the higher resolution method. Here, we show that the resolution of DOI can be greatly improved through localization, where the problem becomes finding the position of a point source [21–23]. The prior information that is incorporated into the inversion is that a measurement data set contains information about only a single fluorescent inhomogeneity. Practically, such measurements could be made, for example, if the inhomogeneities have sufficient separation in space, time, and/or emission spectrum. Furthermore, we model every inhomogeneity as a point source, an assumption that has been shown to be valid numerically and experimentally for fluorescent inhomogeneities with diameters up to 10 mm at depths of 10-20 mm in tissue-simulating 1 % Intralipid [23]. This assumption holds because of the rapid attenuation of high spatial frequencies within the scattering medium. Here, the efficacy of localizing a cylindrical fluorescent inhomogeneity with 1 mm diameter and 2 mm height is demonstrated. With sufficient SNR, smaller inhomogeneities could be localized, and previous work [23] suggests that larger inhomogeneities with diameters of at least 10 mm could also be localized. If needed, the forward model could be modified for structured or larger inhomogeneities [32], extending localization beyond a single point in space.

III. LOCALIZATION FOR SUPER-RESOLUTION

We propose localization as a means for finding fluorescent inhomogeneities embedded within a highly scattering medium with great precision. The method estimates the location of an inhomogeneity by fitting measured intensity data to a diffusion equation forward model for a point emitter, allowing extraction of the 3-D position of the inhomogeneity. For the forward model, we use an analytical solution to the diffusion equation in an infinite slab geometry [1], and we note that analytical solutions can be derived for more complicated geometries [33], or the forward model could be solved using a numerical method [34].

A. Forward Model

Equations (1) and (2) can be used to derive a forward model for comparison with measured data. For experimental simplicity, we set $\omega = 0$, so that the data is an integration over the measured temporal response at each measurement location. As seen in Fig. 2, a single point excitation source corresponding to the laser excitation is positioned at $\mathbf{r}_s$. In this case, $S_x(\mathbf{r}, \omega) = S_o\delta(\mathbf{r} - \mathbf{r_s})$, where S_o is the laser excitation power density (W/mm^3) and δ is the Dirac delta function. Furthermore, N point detectors at λ_m that correspond to camera pixels behind an emission bandpass filter are placed at positions $\mathbf{r}_i$, where i is an index form 1 to N. Finally, in the example we consider, a single fluorescent point source is located at $\mathbf{r}_f$, such that $S_f(\mathbf{r}, \omega) = \eta\mu_{a_f}\delta(\mathbf{r} - \mathbf{r}_f)$, where η is the fluorophore's quantum yield and μ_{a_f} is its absorption. Estimating $\mathbf{r}_f$ constitutes localization. Under these conditions, we let $g_x(\mathbf{r}_s, \mathbf{r}_f)$ represent the Green's function for (1) at λ_x (the excitation wavelength) and $g_m(\mathbf{r}_f, \mathbf{r}_i)$ be the Green's function for (2) at λ_m (the fluorescent wavelength), assuming an infinite slab geometry. Then, the ith element of the forward model vector, describing the fluorescence emission measured at $\mathbf{r}_i$, $\tilde{f}_i$, is

$$\tilde{f}_i(\mathbf{r}_f) = w\left[g_m(\mathbf{r}_f, \mathbf{r}_i)g_x(\mathbf{r}_s, \mathbf{r}_f)\right] \tag{4}$$

$$\equiv wf_i(\mathbf{r}_f), \tag{5}$$

where w is a multiplicative constant that incorporates η, S_o, and the efficiency of light coupling into the medium, and $f_i(\mathbf{r}_f)$ depends nonlinearly on $\mathbf{r}_f$. The excitation laser light incident upon the medium is approximated in the model as an isotropic point source located one mean-free path length ($l^* = 3D$) into the medium [1, 13, 23], where l^* is the distance for photon momentum randomization. Similarly, the light collected by the detectors, in our case each pixel of a camera, is modeled as that given by a diffusion model at points located l^* into the medium. We derive f_i using the extrapolated zero flux boundary conditions shown in Fig. 2 to simulate an infinite homogeneous slab geometry [1]. The extrapolated boundary condition can accommodate mismatched background refractive indices at the surface. We set the extrapolated boundary $l_s = 5.03D$ away from the physical surface, analogous to an interface between air and scatterers in water [35] and useful in our earlier experiments [23], to approximately model the physical boundary for the experimental results we present. Four pairs of excitation and fluorescent image sources are placed to approximately enforce $\phi = 0$ at the extrapolated boundary. Superposition of the physical and image sources allows analytic expressions for $g_x(\mathbf{r}_s, \mathbf{r}_f)$ and $g_m(\mathbf{r}_f, \mathbf{r}_i)$ to be obtained that have the form in (3).

B. Position Estimation

If a fluorescent inhomogeneity is present, which can be determined subject to some probability of detection [23], in order to localize it, we must estimate $\mathbf{r}_f$. This can be accomplished through minimization of the cost function

$$c(\mathbf{r}_f) = \min_{w} ||\mathbf{y} - w\mathbf{f}(\mathbf{r}_f)||^2_{\boldsymbol{\Upsilon}^{-1}} \tag{6}$$

over all $\mathbf{r}_f$ of interest, where $\mathbf{y}$ is a vector of N measurements, $\mathbf{f}(\mathbf{r}_f)$ is a vector of N normalized forward calculations $f_i(\mathbf{r}_f)$, from (5), $\boldsymbol{\Upsilon} = \alpha \text{diag}[|y_1|, \ldots, |y_N|]$ is the noise covariance matrix, for which we assume a Gaussian noise model characterized by α [13], and for an arbitrary vector $\mathbf{v}$, $||\mathbf{v}||^2_{\boldsymbol{\Upsilon}^{-1}} = \mathbf{v}^H \boldsymbol{\Upsilon}^{-1}\mathbf{v}$, where H denotes the Hermitian transpose. A two step procedure can be used to solve this optimization problem [23, 32, 36], where the minimization in (6) with respect to w leads to

$$\tilde{w}(\mathbf{r}_f) = \frac{\mathbf{f}^T(\mathbf{r}_f)\boldsymbol{\Upsilon}^{-1}\mathbf{y}}{\mathbf{f}^T(\mathbf{r}_f)\boldsymbol{\Upsilon}^{-1}\mathbf{f}(\mathbf{r}_f)}, \tag{7}$$

found by taking the derivative with respect to w and setting the result equal to zero, and this estimate results in the modified cost function

$$c(\mathbf{r}_f) = ||\mathbf{y} - \tilde{w}(\mathbf{r}_f)\mathbf{f}(\mathbf{r}_f)||^2_{\boldsymbol{\Upsilon}^{-1}}. \tag{8}$$

The maximum likelihood estimates are then

$$\hat{\mathbf{r}}_f = \arg\min_{\mathbf{r}_f} c(\mathbf{r}_f) \tag{9}$$

$$\hat{w} = \tilde{w}(\hat{\mathbf{r}}_f), \tag{10}$$

where (8) is minimized over a set of values for $\mathbf{r}_f$ bounded by the slab geometry. Therefore, the estimate $\hat{\mathbf{r}}_f$ in (9) is the position within the slab that returns the lowest value of the cost function (8). In our illustrative example of a homogeneous scattering slab, this minimization can be computed quickly because the Green's functions from (4) used to calculate $\mathbf{f}(\mathbf{r}_f)$ are closed-form and given by (3). However, the forward model data could also be generated using finite element or related numerical methods [34], at the cost of increased computational time.

C. Noise Model

A Gaussian noise model is implied by (6), and the use of non-zero elements only on the diagonal of $\boldsymbol{\Upsilon}$ is a consequence of the assumption of independent measurements. The model assumes that each measurement is normally distributed with a mean equal to the noiseless measurement and a variance that is proportional to the DC ($\omega = 0$) component of the noiseless measurement [13]. Simulated noisy data can therefore be numerically generated as

$$\mathrm{Re}[y_i] = \mathrm{Re}[\tilde{f}_i(\mathbf{r}_f)] + [\alpha|\tilde{f}_i(\mathbf{r}_f)|]^{1/2} N(0,1) \tag{11}$$

$$\mathrm{Im}[y_i] = \mathrm{Im}[\tilde{f}_i(\mathbf{r}_f)] + [\alpha|\tilde{f}_i(\mathbf{r}_f)|]^{1/2} N(0,1), \tag{12}$$

where $N(0,1)$ is a zero mean Gaussian random variable with unit variance. The signal-to-noise ratio (SNR in dB) at the ith detector is then

$$\mathrm{SNR}_i = 10\log_{10}\left(\frac{1}{\alpha}|\tilde{f}_i(\mathbf{r}_f)|\right). \tag{13}$$

This noise model assumes that the uncertainty in the estimated position of the fluorescent inhomogeneity ($\hat{\mathbf{r}}_f$) is dominated by measurement noise. This would not be the case, for example, if if the fluorophores changed position or diffused significantly during the integration time of the measurement [37, 38].

IV. RESULTS

A. Simulation and Localization Uncertainty

We first generate 50 noisy independent measurements for an assumed 30 dB SNR using (11) (for $\omega = 0$) to demonstrate the localization of a fluorescent inhomogeneity in a highly scattering slab. Figure 3 shows the geometry we considered, where the positions of an excitation source, a fluorescent inhomogeneity (which is modeled as a point fluorescent source), and $N = 400$ detectors are shown as red, green, and blue points, respectively. The true location of the fluorescent inhomogeneity is $\mathbf{r}_{ft}$, and the slab is 18 mm thick with $\mu_a = 0$ and $\mu_s' = 0.9$ mm^{-1}. A region of interest of size $2 \times 2 \times 1.8$ cm^3 was discretized into a 3-D grid. Following the localization procedure of Section III B, $\tilde{w}(\mathbf{r}_f)$ from (7) and then $c(\mathbf{r}_f)$ from (8) were evaluated at each grid point. Values for $\hat{\mathbf{r}}_f$ and $\hat{w}$ were then calculated using (9) and then (10). Example simulation results are presented in Appendix A, along with a multiresolution method that proved to be computationally efficient. We used this multiresolution approach to localize the fluorescent inhomogeneity and achieve SRDOI.

Because the measurements are noisy, each localized position $\hat{\mathbf{r}}_f$ falls within an underlying probability distribution function $p(\mathbf{r}_f)$ with mean $\mu = \mathbf{r}_{ft}$ and variance σ^2. The performance of the localization can therefore be evaluated by estimating σ, the localization uncertainty [37–39]. By the central limit theorem, σ can be estimated from a sufficient number of samples of $p(\mathbf{r}_f)$ [40]. Therefore, $\hat{\sigma}_x$, $\hat{\sigma}_y$, and $\hat{\sigma}_z$ can be calculated, which are the estimates of σ corresponding to each of the (x, y, z) coordinates of $\mathbf{r}_f$. The same geometry, optical properties, $\mathbf{r}_s$, $\mathbf{r}_i$, and $\mathbf{r}_f$ as in Fig. 3 were used to obtain numerical samples of $p(\mathbf{r}_f)$ as follows. Each simulated measurement data set was then used to determine $\hat{\mathbf{r}}_f$ using (9) with multiresolution. Finally, $\hat{\sigma}_x$, $\hat{\sigma}_y$, and $\hat{\sigma}_z$, were calculated from the 50 values of $\hat{\mathbf{r}}_f$. The results from this statistical analysis are shown in Fig. 4. The depth of the fluorescent inhomogeneity, or its distance from the detector plane, was 13 mm, as shown in Fig. 3. Figure 4(a) gives plots of $\hat{\sigma}_x$, $\hat{\sigma}_y$, and $\hat{\sigma}_z$ versus SNR, and Fig. 4(b) shows a subset of this data as ellipses, where the major and minor axes have dimension $4\hat{\sigma}_x$ or $4\hat{\sigma}_y$. We chose $4\hat{\sigma}_x$ and $4\hat{\sigma}_y$ to indicate the space containing 95% of the localized points. Figure 4(c) presents plots of $\hat{\sigma}_x$, $\hat{\sigma}_y$, and $\hat{\sigma}_z$ versus depth for a constant SNR of 30 dB, and Fig. 4(d) shows plots of ellipses for different depths. It is clear that $\hat{\sigma}_z$ is consistently larger than $\hat{\sigma}_x$ and $\hat{\sigma}_y$. This occurs because the detectors are on a constant z-plane. The value of $\hat{\sigma}_z$ could be reduced to the levels of $\hat{\sigma}_x$ and $\hat{\sigma}_y$ by placing additional detectors in the $x - z$ or $y - z$ planes. Thus, $\hat{\sigma}_x$ and $\hat{\sigma}_y$ are better indicators of the achievable localization uncertainty for the geometry in Fig. 3. The reason $\hat{\sigma}_x$ does not equal $\hat{\sigma}_y$ and the ellipses are not perfect circles is because of the uncertainty in the estimations and the fact that the 400 detectors locations in Fig. 3 are not perfectly symmetric around the fluorescent inhomogeneity. Even though we use the same equation for the forward model that was used to generate the simulated data, it is not guaranteed that the localization will work due to the addition of simulated noise. In the next section we will validate our localization scheme with experimental data and demonstrate that the simulated results closely match those from the experiment.

B. Experiment

We present the results of an experimental study of the accuracy of SRDOI with measurement data collected using the arrangement shown in Fig. 5(a). A highly scattering slab of thickness $d = 18$ mm was created by stacking three pieces of white plastic (Cyro Industries, Acrylite FF, a clear acrylic with 50 nm TiO_2 scatterers) with dimensions $140 \times 140 \times 6$ mm. A hole with a diameter of 1 mm and a depth of 2 mm was drilled into the top-center of the bottom slab. The size of this hole is large relative to the expected localization uncertainty, however it is small enough to be well approximated by a fluorescent point source in a heavily scattering medium [23]. A 10 mM stock of the fluorophore Maleimide ATTO 647N (peak $\lambda_x = 646$ nm, peak $\lambda_m = 664$ nm) in dimethyl sulfoxide (DMSO) was used to prepare a 10 μM diluted solution of the fluorophore. This fluorophore solution was carefully placed into the drilled hole in the bottom highly scattering slab using a pipette and a needle to remove air bubbles.

The filtered output of a pulsed supercontinuum source (EXR-20 NKT Photonics, 5 ps seed pulse width, 20 MHz repetition rate, VARIA tunable filter) was used to generate the excitation light at $\lambda_x = 633$ nm with a 10 nm bandwidth, as shown in Fig. 5(a). With this bandwidth, the average excitation power was approximately 15 mW. Measurements at $\lambda_m = 676$ nm were made through an OD6 bandpass filter having a bandwidth of 29 nm (Edmund Optics 86-996), to reject the excitation light. Measurements at λ_x were performed by removing the bandpass filter. All measurements were pseudo-CW (corresponding to unmodulated light data and $\omega = 0$ in (1) and (2)), with the CCD camera (PIMAX, 512 x 512 pixels) integration time being long compared to the pulsed laser repetition rate (20 MHz). A λ_x measurement result with an integration time of 30 ms is shown in Fig. 5(b).

All λ_m measurements were calibrated by subtracting corresponding measurements of the filter bleed-through, according to $y_i = y_i^{slab} - y_i^{bleed}$, where y_i is the ith component of $\mathbf{y}$, y_i^{slab} is the ith experimental datum captured from the slab, and y_i^{bleed} is the ith experimental datum from the slab without the fluorescent inhomogeneity present. A calibrated λ_m measurement with an integration time of 1 s is shown in Fig. 5(c). We selected $N = 400$ detector locations (pixels) around the maximum value, as shown by the blue dots. The values (indicated by the color bar) at these positions were used to construct the data vector $\mathbf{y}$ in (6).

In order to calculate the forward solution in (4), μ_s', μ_a, $\mathbf{r}_i$ for each detector along with $\mathbf{r}_s$ must be known. To determine these, first the positions of all pixels in Fig. 5(b) and (c) were found in mm using images of a ruler like that shown in Fig. 5(d). Care was taken in the alignment of the experimental components so that the distance between each pixel in the x and y dimensions was approximately the same (0.043 mm). The x_i and y_i coordinates of the vector $\mathbf{r}_i$ could then be determined from the positions of the chosen 400 detector pixels, and the z coordinate was $(18 - 3D)$ mm, to satisfy the zero-flux boundary condition at the top of the scattering medium [1]. The point directly below the maximum intensity in Fig. 5(b) indicates the source position, $\mathbf{r}_s$. This position of maximum intensity was estimated by fitting a 2-D Gaussian function [37] to Fig. 5(b). This procedure resulted in $\mathbf{r}_s = (8.09, 9.07, 3D)$ mm, where the z component is $3D$ to satisfy the boundary condition at the bottom of the scattering medium [1]. The 2-D Gaussian fit was also used to estimate the true location of the fluorescent inhomogeneity using a data set with 50 times the integration time of that used for Fig. 5(c), resulting in a much higher SNR than that of Fig. 5(c). The true location was estimated as the centroid with coordinates $\mathbf{r}_{ft} = (12.77, 10.79, 5.0)$ mm, where the z component at the center of the drilled hole was found from the thickness of the white plastic slabs (6 mm) and the depth of the drilled hole (2 mm). We note that the 2-D Gaussian fit does not provide depth information, motivating the use of the localization method in Section III even in this simple example.

The optical parameters of the slab, μ_s' and μ_a, were estimated by fitting (3) to the data shown in Fig. 5(b), where in this case, $\mathbf{r}' = \mathbf{r}_s$, $\mathbf{r} = \mathbf{r}_i$, and the z components of $\mathbf{r}_s$ and $\mathbf{r}_i$ depended on μ_s' and μ_a. The data in Fig. 5(b) was captured with the fluorescent inhomogeneity present, but because the bandpass filter used in the experiment attenuated the excitation light by a factor of 10^6, the fluorescent signal in Fig. 5(b) was assumed to be negligible compared to the transmitted excitation light. It was also assumed that the scattering medium background exists throughout the small volume occupied by the fluorophore. The scattering slabs used have very low absorption in the wavelength range for these experiments, so we set $\mu_a = 0$. The estimated μ_s' of the slab (at 633 nm) was found to be 0.9 mm^{-1}, giving $3D = 1.111$ mm. These values are within the uncertainty of previous estimates using the same method [41]. The positions $\mathbf{r}_s$, $\mathbf{r}_i$, and $\mathbf{r}_{ft}$, are those indicated in Fig. 3, and were used for the corresponding numerical simulations in Appendix A and Fig. 4, so that the simulation and experimental results can be compared.

The forward solution calculated in (4) using the experimental parameters, along with the experimental measurement vector $\mathbf{y}$, allow localization of the fluorescent inhomogeneity embedded in the highly scattering slab. In order to characterize the experimental localization uncertainty, the λ_m measurement shown in Fig. 5(c) was repeated 50 times. Localization using these 50 measurements then allows calculation of the experimental $\hat{\sigma}_x$, $\hat{\sigma}_y$, and $\hat{\sigma}_z$. The resulting values are shown plotted as an ellipse in Fig. 6(a), with an axial ratio of $\hat{\sigma}_y/\hat{\sigma}_x = 0.0232/0.0229$ (i.e., close to circular), and presented in Table I.

In order to validate the SRDOI method, the experimental results in Fig. 6(a) can be compared to the numerical data in Fig. 4. These results were all generated using the same $\mathbf{r}_s$, $\mathbf{r}_i$, and $\mathbf{r}_{ft}$, and identical scattering medium optical parameters, μ_s' and D. In order to estimate the SNR of the experiment, we calculated the ML estimate of the noise parameter α from the full form of (6) [42], giving

$$\hat{\alpha} = \frac{1}{N}||\mathbf{y} - \hat{w}\mathbf{f}(\hat{\mathbf{r}}_f)||^2_{\tilde{\mathbf{\Upsilon}}^{-1}}, \tag{14}$$

where $\tilde{\mathbf{\Upsilon}} = \text{diag}[|y_1|, \ldots, |y_N|]$ uses measured data. The SNR of the ith detector was then estimated using (13) as

$$\text{SNR}_i = 10\log_{10}\left(\frac{1}{\hat{\alpha}}|\hat{w}f_i(\hat{\mathbf{r}}_f)|\right). \tag{15}$$

The SNR was calculated for all 400 detectors using (15) and one of the 50 experimental data sets and its corresponding values for $\hat{w}$ and $\hat{\mathbf{r}}_f$. The mean experimental SNR was found to be 28.9 dB, its standard deviation across detectors was 0.62 dB, and its maximum was 29.9 dB. We used this mean SNR to generate the blue ellipse in Fig. 6(b), which is plotted with the red ellipse from Fig. 6(a). The values for the numerical localization uncertainties are also presented in Table I. Note that the experimental and numerical uncertainties are close, signifying that (13) describes the noise process well. The difference between the experimental mean and the true location is likely due to the fit approximation used to determine the true location and estimation error.

C. Resolution

A natural way to compare the localization uncertainties to the resolution of diffuse optical imaging is to calculate the FWHM of the density function $p(\mathbf{r}_f)$ that describes the localized positions. For a localization uncertainty σ and a Gaussian spread of localized points, we can write the resolution as

$$\text{Resolution} = 2\sqrt{2\ln 2}\,\sigma \approx 2.36\,\sigma, \tag{16}$$

corresponding to the full width at one half of the maximum. The numerical and experimental results are summarized in Table I for the case of depth = 13 mm, as shown in Fig. 3, and a mean SNR of 28.9 dB, found for the experiment. The $\hat{\mu}_x$, $\hat{\mu}_y$, and $\hat{\mu}_z$ are the mean of the localized position components. The FDOT resolution is estimated as depth/2.

V. DISCUSSION

We have developed a localization method that allows imaging of fluorescent inhomogeneities deep in heavily scattering media with unprecedented spatial resolution. The method was validated numerically and experimentally, demonstrating an improvement of two orders of magnitude in resolution compared to DOI. An analytic forward solution in an infinite slab geometry was used, but analytic solutions could be derived for arbitrary geometries using the Kirchhoff approximation [33]. Alternatively, numerical methods such as the finite element method could be used to solve the forward problem for inhomogeneous media, where DOT could be employed to determine μ_s' and μ_a [43, 44]. However, the limited resolution to which μ_s' and μ_a could be estimated with DOT in inhomogeneous media may increase the localization uncertainty. The localization constraints could be incorporated into the FDOT framework [17, 45], potentially allowing reconstruction of super-resolution images. Also, (6) could be minimized using alternative optimization methods, such as a gradient search.

The diffusion model presented in (1) and (2) assumes that the photon current density does not change over one transport mean free path, $l^* = 3D$. For the white plastic slab used here, $l^* = 1.11$ mm at 633 nm, which is much larger than the localization uncertainties in Table I. Therefore, SRDOI can find a fluorescent inhomogeneity with a resolution that is much less than the minimum length described by the physics in the diffusion model. This is possible because of the prior information that has been incorporated into the localization. The results suggest that the localization uncertainty is dominated by measurement noise and not inaccuracies in the model. Therefore, a more accurate model, such as the radiative transfer equation (RTE), is not required unless the combination of the diffusion equation forward model and the prior information is insufficient for accurate localization. This could be the case with weak scatter or high absorption, for example.

We found that a single excitation source position, $\mathbf{r}_s$, was sufficient for the situation considered, which is practical for experimentation. However, multiple excitation source positions or expanded beam excitation may increase the fluorescence emission and reduce the localization uncertainty. A low-pass spatial filter could be applied to the experimental data before estimating $\mathbf{r}_f$ in order to further reduce the localization uncertainty (results not shown). This would smooth the noisy experimental data prior to the localization. The computational time could be reduced and the experiment simplified by using fewer detectors [23]. A few sensitive photodetectors placed at the surface of a scattering medium should be sufficient to localize an inhomogeneity with higher SNR than what can be achieved with a CCD camera. Figure 5(a) shows a transmission measurement, but a reflection measurement could be performed. Also, the localization uncertainty may be reduced through the use of modulated light (non-zero ω). For *in vivo* applications, longer wavelengths may improve the SNR due to lower light absorption in tissue.

Practical application of SRDOI requires access to fluorescent light data that can be assumed to originate from single fluorescent inhomogeneities. This could be accomplished through known variations in space, time, the fluorescence emission spectrum, or a combination of these. Variation in space could simply be fluorescent inhomogeneities separated by distances greater than the FWHM of the PSF. Variation in time could be a unique temporal delay for each inhomogeneity, where measurements with short integration times (and sufficient SNR) could allow separation of the temporal responses. Finally, if each inhomogeneity emitted photons at different energies, a spectral measurement could allow separation of each response. All of these variations are possible with blinking quantum dots of different diameters [46], where each quantum dot could then be localized in deep tissue.

Localization techniques have also been developed in microscopy for improving resolution [47, 48]. For example, in stochastic optical reconstruction microscopy (STORM) [49], a subset of fluorescent molecules that are separated by a distance greater than the diffraction limit are switched between fluorescent and non-fluorescent states. Each molecule is then located with an uncertainty that is much less than the diffraction limit. With multiple measurements, a super-resolution image is formed by combining many localized positions. However, this is a fundamentally different class of problem where scatter is largely ignored and the imaging system objective function is incorporated into the localization framework. In our case, a model for the heavily scattering domain is used in an optimization-based localization framework. Interestingly, the improvement in spatial resolution that is achieved with super-resolution in microscopy is comparable to what is achieved by SRDOI. For example, a diffraction-limited resolution of 200 nm is improved to a few nanometers when imaging single fluorescent molecules [50], an improvement of about two orders in magnitude. The localization technique presented here enables super-resolution imaging in other physical imaging problems that use forward models, such as photoacoustic tomography [51], electrical impedance tomography [52], seismic waveform tomography [53], and microwave imaging [54]. While the experiments differ, the premise we presented should apply.

One potential application of SRDOI is brain imaging [55–57]. Signaling between neurons is accompanied by an increase in the local concentration of calcium, which can modulate the emission of fluorophores within the brain [58, 59]. Each neuron can be treated as a fluorescent inhomogeneity that, for example, emits photons when the neuron fires. In this case, measurements by a CCD camera or a fiber array with an appropriate integration time could provide data from individual neurons to allow each neuron or a set of neurons to be localized. In principle, this could provide an image of a whole animal brain or the brain surface *in vivo* at a resolution of tens of micrometers. These images would provide new information on how the brain encodes perceived information into chemical and electrical neural activity, and how local neural circuits interact with different brain areas. Correlation maps with such data should prove useful for studying neurological diseases and developing treatments [60].

VI. CONCLUSION

We have introduced a new diffuse optical imaging modality where the positions of inhomogeneities embedded in highly scattering tissue-like media are estimated in order to achieve high spatial resolution through localization. Examples of inhomogeneities include biological structures such as cells that are stained with targeted fluorescent contrast agents. Therefore, the SRDOI localization approach enables designed fluorescent studies of biochemical processes in deep tissue and *in vivo*. Alternatively, absorbing inhomogeneities that do not fluoresce could be localized [32, 36]. We demonstrated the capability of SRDOI numerically and experimentally by localizing a fluorescent inhomogeneity at a depth of 13 mm in a highly scattering slab. The localization uncertainty was characterized in order to understand the limits to which the location of the inhomogeneity could be estimated. From this uncertainty, we found that SRDOI can achieve a spatial resolution better than tens of microns, an improvement of over two orders of magnitude compared to DOI methods such as FDOT. This is the first super-resolution optical imaging method with the potential of deep *in vivo* imaging, and can be applied to a broad class of physical problems that use forward models, addressing a critical need in biomedical imaging for deep-tissue high resolution optical imaging.

VII. ACKNOWLEDGMENT

This work was funded in part by the National Science Foundation (CISE-1218909) and the National Institutes of Health (1R21CA182235-01A1). This paper describes objective technical results and analysis. Any subjective views or opinions that might be expressed in the paper do not necessarily represent the views of the U.S. Department of Energy or the United States Government.

Appendix A: Localization with a Multiresolution Approach

In this Appendix, simulation examples of the localization methods used to generate the results are presented. Consider a region of interest of size $2 \times 2 \times 1.8$ cm^3, as defined in Section IV A. The localization procedure described in Section III B was performed on the discretized region of interest with $N_x = 17$ points in the x dimension, $N_y = 17$ points in the y

dimension, and $N_z = 17$ points in the z dimension. Figures 7(a) and (b) show plots of $\tilde{w}(\mathbf{r}_f)$ and $c(\mathbf{r}_f)$ for a fixed y such that the plots contain the minimum of $c(\mathbf{r}_f)$. The estimated location of the fluorescent point source $\hat{\mathbf{r}}_f$ can then be determined. The localization error was calculated as $[(\mathbf{r}_{ft} - \hat{\mathbf{r}}_f)/\mathbf{r}_{ft} \times 100]\%$, and the error in Figs. 7(a) and (b) is relatively high because of the spatial grid discretization over the region of interest.

In order to achieve high resolution, the grid spacing of the points within the region of interest must be reduced from what is used in Figs. 7(a) and (b). However, this presents a computational problem when evaluating $\tilde{w}(\mathbf{r}_f)$ and $c(\mathbf{r}_f)$, because (4) must be calculated for each combination of $\mathbf{r}_i$ and $\mathbf{r}_f$ within the region of interest. For this reason, we apply a multiresolution method to simultaneously reduce the computational time and the discretization error of the localization. This multiresolution approach is similar to multigrid in the general sense that it incorporates a hierarchy of discretization grids into the localization [42, 61, 62]. However, multigrid algorithms propagate solutions back and forth between coarse and fine grids to reduce errors, whereas our multiresolution approach iterates strictly in one direction from coarse to finer grids. Therefore, we use the term multiresolution to describe the method, which is demonstrated in Fig. 7(c). First, the cost $c(\mathbf{r}_f)$ is calculated and minimized in the region of interest with dimensions $2 \times 2 \times 1.8$ cm^3, as before, but with a grid of $N_x = N_y = N_z = 5$. The cost is then iteratively calculated on successively smaller regions of interest that each encompass the point of minimum cost found from the previous iteration. At each iteration after the first, the region of interest extends a distance equal to the grid spacing of the previous iteration along each dimension around the point of minimum cost, and the grid contains the same number of gird points ($5 \times 5 \times 5$). This procedure is repeated until convergence, which we defined as two grids where the change in the minimum cost was less than 0.1%, but not equal to zero. In Fig. 7(c), the first three iterations are shown. It is observed that successive iterations appear to “zoom in” on the point of lowest cost. After 13 iterations, the convergence condition was satisfied and $\hat{\mathbf{r}}_f$ was calculated using (9). The localization error is much less than that of Fig. 7(a) and (b) because multiresolution has effectively minimized the discretization error. Multiresolution was important in achieving the results in Section IV because it substantially reduced the computational times.

[1] Michael S Patterson, Britton Chance, and Brian C Wilson, "Time resolved reflectance and transmittance for the non-invasive measurement of tissue optical properties," Ann. Phys. (NY) **28**, 2331–2336 (1989).

[2] M. A. OLeary, D. A. Boas, B. Chance, and A. G. Yodh, "Refraction of diffuse photon density waves," Phys. Rev. Lett. **69**, 2658 (1992).

[3] AP Gibson, JC Hebden, and Simon R Arridge, "Recent advances in diffuse optical imaging," Phys. Med. Biol. **50**, R1 (2005).

[4] Ernst Abbe, "Beiträge zur theorie des mikroskops und der mikroskopischen wahrnehmung," Arch. Mikr. Anat. **9**, 413–418 (1873).

[5] Roarke Horstmeyer, Haowen Ruan, and Changhuei Yang, "Guidestar-assisted wavefront-shaping methods for focusing light into biological tissue," Nat. Photon. **9**, 563–571 (2015).

[6] S M Popoff, G Lerosey, R Carminati, M Fink, A C Boccara, and S Gigan, "Measuring the transmission matrix in optics: an approach to the study and control of light propagation in disordered media," Phys. Rev. Lett. **104**, 100601 (2010).

[7] Matthieu Davy, Zhou Shi, and Azriel Z Genack, "Focusing through random media: Eigenchannel participation number and intensity correlation," Phys. Rev. B **85**, 035105 (2012).

[8] Thomas Chaigne, Jérôme Gateau, Ori Katz, Emmanuel Bossy, and Sylvain Gigan, "Light focusing and two-dimensional imaging through scattering media using the photoacoustic transmission matrix with an ultrasound array," Opt. Lett. **39**, 2664–2667 (2014).

[9] Jason A Newman and Kevin J Webb, "Imaging optical fields through heavily scattering media," Phys. Rev. Lett. **113**, 263903 (2014).

[10] Jason A Newman, Qiaoen Luo, and Kevin J Webb, "Imaging hidden objects with spatial speckle intensity correlations over object position," Phys. Rev. Lett. **116**, 073902 (2016).

[11] C P Gonatas, Masaru Ishii, John S Leigh, and John C Schotland, "Optical diffusion imaging using a direct inversion method," Phys. Rev. E **52**, 4361 (1995).

[12] Jorge Ripoll, Ralf B Schulz, and Vasilis Ntziachristos, "Free-space propagation of diffuse light: theory and experiments," Phys. Rev. Lett. **91**, 103901 (2003).

[13] J. C. Ye, K. J. Webb, C. A. Bouman, and R. P. Millane, "Optical diffusion tomography by

iterative coordinate descent optimization in a Bayesian framework," J. Opt. Soc. Am. A **16**, 2400–2412 (1999).

[14] David L Everitt, S P Wei, and X D Zhu, "Analysis and optimization of a diffuse photon optical tomography of turbid media," Phys. Rev. E **62**, 2924 (2000).

[15] Vadim A Markel and John C Schotland, "Symmetries, inversion formulas, and image reconstruction for optical tomography," Phys. Rev. E **70**, 056616 (2004).

[16] Vasilis Ntziachristos and Ralph Weissleder, "Charge-coupled-device based scanner for tomography of fluorescent near-infrared probes in turbid media," Med. Phys. **29**, 803–809 (2002).

[17] A. B. Milstein, S. Oh, K. J. Webb, C. A. Bouman, Q. Zhang, D. A. Boas, and R. P. Millane, "Fluorescence optical diffusion tomography," Appl. Opt. **42**, 3081–3094 (2003).

[18] Esther H R Tsai, Brian Z Bentz, Venkatesh Chelvam, Vaibhav Gaind, Kevin J Webb, and Philip S Low, "*In vivo* mouse fluorescence imaging for folate-targeted delivery and release kinetics," Biomed. Opt. Express **5**, 2662–2678 (2014).

[19] Wouter Peelaerts, Luc Bousset, Anke Van der Perren, Anastacia Moskalyuk, Rocco Pulizzi, Michele Giugliano, Chris Van den Haute, Ronald Melki, and Veerle Baekelandt, "α-synuclein strains cause distinct synucleinopathies after local and systemic administration," Nature **522**, 340–344 (2015).

[20] Vasilis Ntziachristos, Jorge Ripoll, Lihong V Wang, and Ralph Weissleder, "Looking and listening to light: the evolution of whole-body photonic imaging," Nat. Biotechnol. **23**, 313–320 (2005).

[21] Edward L Hull, Michael G Nichols, and Thomas H Foster, "Localization of luminescent inhomogeneities in turbid media with spatially resolved measurements of CW diffuse luminescence emittance," Appl. Opt. **37**, 2755–2765 (1998).

[22] Marcus Pfister and Bernhard Scholz, "Localization of fluorescence spots with space-space music for mammographylike measurement systems," J. Biomed. Opt. **9**, 481–487 (2004).

[23] Adam B Milstein, Michael D Kennedy, Philip S Low, Charles A Bouman, and Kevin J Webb, "Statistical approach for detection and localization of a fluorescing mouse tumor in Intralipid," Appl. Opt. **44**, 2300–2310 (2005).

[24] Jean-Pierre LHuillier and Fabrice Vaudelle, "Improved localization of hidden fluorescent objects in highly scattering slab media based on a two-way transmittance determination," Opt. Exp. **14**, 12915–12929 (2006).

[25] Y Chen, G Zheng, ZH Zhang, D Blessington, M Zhang, H Li, Q Liu, L Zhou, X Intes, S Achilefu, and B Chance, "Metabolism-enhanced tumor localization by fluorescence imaging: *in vivo* animal studies," Opt. Lett. **28**, 2070–2072 (2003).

[26] XD Li, MA O'Leary, DA Boas, Britton Chance, and AG Yodh, "Fluorescent diffuse photon density waves in homogeneous and heterogeneous turbid media: analytic solutions and applications," Appl. Opt. **35**, 3746–3758 (1996).

[27] J Ripoll, M Nieto-Vesperinas, and Rémi Carminati, "Spatial resolution of diffuse photon density waves," J. Opt. Soc. Am. A **16**, 1466–1476 (1999).

[28] Brian W Pogue, Troy O McBride, Ulf L Osterberg, and Keith D Paulsen, "Comparison of imaging geometries for diffuse optical tomography of tissue," Opt. Exp. **4**, 270–286 (1999).

[29] DA Boas, K Chen, D Grebert, and MA Franceschini, "Improving the diffuse optical imaging spatial resolution of the cerebral hemodynamic response to brain activation in humans," Opt. Lett. **29**, 1506–1508 (2004).

[30] Brian W Pogue and Keith D Paulsen, "High-resolution near-infrared tomographic imaging simulations of the rat cranium by use of a priori magnetic resonance imaging structural information," Opt. Lett. **23**, 1716–1718 (1998).

[31] Vasilis Ntziachristos, AG Yodh, Mitchell D Schnall, and Britton Chance, "MRI-guided diffuse optical spectroscopy of malignant and benign breast lesions," Neoplasia **4**, 347–354 (2002).

[32] Brian Z Bentz, Timothy C Wu, Vaibhav Gaind, and Kevin J Webb, "Diffuse optical localization of blood vessels and 3D printing for guiding oral surgery," Appl. Opt. **56**, 6649–6654 (2017).

[33] Jorge Ripoll, Vasilis Ntziachristos, Remi Carminati, and Manuel Nieto-Vesperinas, "Kirchhoff approximation for diffusive waves," Phys. Rev. E **64**, 051917 (2001).

[34] Martin Schweiger and Simon Arridge, "The Toast++ software suite for forward and inverse modeling in optical tomography," J. Biomed. Opt. **19**, 040801–040801 (2014).

[35] Richard C Haskell, Lars O Svaasand, Tsong-Tseh Tsay, Ti-Chen Feng, Bruce J Tromberg, and Matthew S McAdams, "Boundary conditions for the diffusion equation in radiative transfer," J. Opt. Soc. Am. A **11**, 2727–2741 (1994).

[36] Guangzhi Cao, Vaibhav Gaind, Charles A Bouman, and Kevin J Webb, "Localization of an absorbing inhomogeneity in a scattering medium in a statistical framework," Opt. Lett. **32**, 3026–3028 (2007).

[37] Russell E Thompson, Daniel R Larson, and Watt W Webb, "Precise nanometer localization analysis for individual fluorescent probes," Biophys. J. **82**, 2775–2783 (2002).

[38] Xavier Michalet, "Mean square displacement analysis of single-particle trajectories with localization error: Brownian motion in an isotropic medium," Phys. Rev. E **82**, 041914 (2010).

[39] Francisco Balzarotti, Yvan Eilers, Klaus C Gwosch, Arvid H Gynnå, Volker Westphal, Fernando D Stefani, Johan Elf, and Stefan W Hell, "Nanometer resolution imaging and tracking of fluorescent molecules with minimal photon fluxes," Science **355**, 606–612 (2017).

[40] Athanasios Papoulis and S Unnikrishna Pillai, *Probability, Random Variables, and Stochastic Processes* (Tata McGraw-Hill Education, 2002).

[41] Charles A Thompson, Kevin J Webb, and Andrew M Weiner, "Diffusive media characterization with laser speckle," Appl. Opt. **36**, 3726–3734 (1997).

[42] Jong Chul Ye, Charles A Bouman, Kevin J Webb, and Rick P Millane, "Nonlinear multigrid algorithms for Bayesian optical diffusion tomography," IEEE Trans. Image Process. **10**, 909–922 (2001).

[43] Martin Schweiger, Simon R Arridge, and David T Delpy, "Application of the finite-element method for the forward and inverse models in optical tomography," J. Math. Imaging Vision **3**, 263–283 (1993).

[44] Jenni Heino, Simon Arridge, Jan Sikora, and Erkki Somersalo, "Anisotropic effects in highly scattering media," Phys. Rev. E **68**, 031908 (2003).

[45] Vivian Pera, Eric Zettergren, Dana H Brooks, and Mark Niedre, "Maximum likelihood tomographic reconstruction of extremely sparse solutions in diffuse fluorescence flow cytometry," Opt. Lett. **38**, 2357–2359 (2013).

[46] Ken T Shimizu, Robert G Neuhauser, Catherine A Leatherdale, Stephen A Empedocles, W K Woo, and Moungi G Bawendi, "Blinking statistics in single semiconductor nanocrystal quantum dots," Phys. Rev. B **63**, 205316 (2001).

[47] Eric Betzig, George H Patterson, Rachid Sougrat, O Wolf Lindwasser, Scott Olenych, Juan S Bonifacino, Michael W Davidson, Jennifer Lippincott-Schwartz, and Harald F Hess, "Imaging intracellular fluorescent proteins at nanometer resolution," Science **313**, 1642–1645 (2006).

[48] Samuel T Hess, Thanu PK Girirajan, and Michael D Mason, "Ultra-high resolution imaging by fluorescence photoactivation localization microscopy," Biophys. J. **91**, 4258–4272 (2006).

[49] Michael J Rust, Mark Bates, and Xiaowei Zhuang, "Sub-diffraction-limit imaging by stochas-

tic optical reconstruction microscopy (storm)," Nat. Meth. **3**, 793–796 (2006).

[50] Hans Blom and Jerker Widengren, "Stimulated emission depletion microscopy," Chem. Rev. (2017).

[51] Minghua Xu and Lihong V Wang, "Universal back-projection algorithm for photoacoustic computed tomography," Phys. Rev. E **71**, 016706 (2005).

[52] Margaret Cheney, David Isaacson, and Jonathan C Newell, "Electrical impedance tomography," SIAM review **41**, 85–101 (1999).

[53] R Gerhard Pratt, "Seismic waveform inversion in the frequency domain, Part 1: Theory and verification in a physical scale model," Geophysics **64**, 888–901 (1999).

[54] Tonny Rubæk, Paul M Meaney, Peter Meincke, and Keith D Paulsen, "Nonlinear microwave imaging for breast-cancer screening using gauss–newton's method and the CGLS inversion algorithm," IEEE T. Antenn. Propag. **55**, 2320–2331 (2007).

[55] Michael Scherg, "Functional imaging and localization of electromagnetic brain activity," Brain Topogr. **5**, 103–111 (1992).

[56] Robert Prevedel, Young-Gyu Yoon, Maximilian Hoffmann, Nikita Pak, Gordon Wetzstein, Saul Kato, Tina Schrödel, Ramesh Raskar, Manuel Zimmer, Edward S Boyden, and Alipasha Vaziri, "Simultaneous whole-animal 3D imaging of neuronal activity using light-field microscopy," Nat. Meth. **11**, 727–730 (2014).

[57] Adam T Eggebrecht, Silvina L Ferradal, Amy Robichaux-Viehoever, Mahlega S Hassanpour, Hamid Dehghani, Abraham Z Snyder, Tamara Hershey, and Joseph P Culver, "Mapping distributed brain function and networks with diffuse optical tomography," Nat. Photon. **8**, 448–454 (2014).

[58] Ryohei Yasuda, Esther A Nimchinsky, Volker Scheuss, Thomas A Pologruto, Thomas G Oertner, Bernardo L Sabatini, and Karel Svoboda, "Imaging calcium concentration dynamics in small neuronal compartments," Sci. STKE **2004**, pl5 (2004).

[59] Michael Lawrence Castanares, Vini Gautam, Jack Drury, Hans Bachor, and Vincent R Daria, "Efficient multi-site two-photon functional imaging of neuronal circuits," Biomed. Opt. Express **7**, 5325–5334 (2016).

[60] Ed Bullmore and Olaf Sporns, "Complex brain networks: graph theoretical analysis of structural and functional systems," Nature Rev. Neurosci. **10**, 186–198 (2009).

[61] A Brandt, *Multigrid Techniques: 1984 Guide, with Applications to Fluid Dynamics* (Sankt

Augustin, Germany: GMD-Studien, 1984).

[62] Seungseok Oh, Charles A Bouman, and Kevin J Webb, "Multigrid tomographic inversion with variable resolution data and image spaces," IEEE Trans. Image Process. **15**, 2805–2819 (2006).

[63] Lingling Zhao, Vivian K Lee, Seung-Schik Yoo, Guohao Dai, and Xavier Intes, "The integration of 3-D cell printing and mesoscopic fluorescence molecular tomography of vascular constructs within thick hydrogel scaffolds," Biomaterials **33**, 5325–5332 (2012).

[64] Edward E Graves, Jorge Ripoll, Ralph Weissleder, and Vasilis Ntziachristos, "A submillimeter resolution fluorescence molecular imaging system for small animal imaging," Med. Phys. **30**, 901–911 (2003).

[65] Samuel Bélanger, Maxime Abran, Xavier Intes, Christian Casanova, and Frederic Lesage, "Real-time diffuse optical tomography based on structured illumination," J. Biomed. Opt. **15**, 016006–016006 (2010).

[66] Guy Satat, Barmak Heshmat, Dan Raviv, and Ramesh Raskar, "All photons imaging through volumetric scattering," Sci. Rep. **6** (2016).

[67] Xiaoqing Zhou, Ying Fan, Qiang Hou, Huijuan Zhao, and Feng Gao, "Spatial-frequency-compression scheme for diffuse optical tomography with dense sampling dataset," Appl. Opt. **52**, 1779–1792 (2013).

[68] JA Moon, R Mahon, MD Duncan, and J Reintjes, "Resolution limits for imaging through turbid media with diffuse light," Opt. Lett. **18**, 1591–1593 (1993).

[69] XD Li, T Durduran, AG Yodh, B Chance, and DN Pattanayak, "Diffraction tomography for biochemical imaging with diffuse-photon density waves," Opt. Lett. **22**, 573–575 (1997).

[70] AH Gandjbakhche, R Nossal, and RF Bonner, "Resolution limits for optical transillumination of abnormalities deeply embedded in tissues," Med. Phys. **21**, 185–191 (1994).

FIGURES

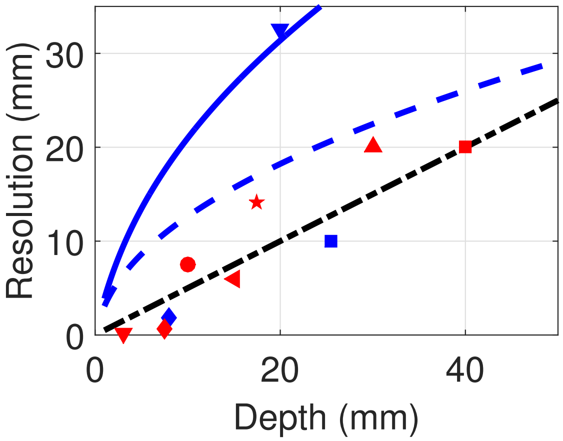

FIG. 1. Resolution of diffuse optical imaging as reported in the literature. Red symbols are image reconstructions, where ▼, ♦, ●, ◀, ★, ▲, and ■, correspond to [28, 29, 63–67]. Blue symbols are direct measurements (no inversion was performed), where ♦, ▼ and ■ correspond to [68–70]. The background μ_s' and μ_a used in each paper varies, but their average values are 0.85 mm^{-1} and 0.0063 mm^{-1} (close to those of tissue-simulating Intralipid), where μ_s' is between 0.5 and 1.0 mm^{-1} and μ_a is between 0 and 0.01 mm^{-1}. The blue curves are theoretical resolution limits for CW ($\omega = 0$) direct measurements, as calculated by Ripoll *et al.* [27]. The dashed blue curve was calculated using breast tissue parameters, where $\mu_s' = 1.5$ mm^{-1} and $\mu_a = 0.0035$ mm^{-1}. The solid blue curve was calculated using the average values from the literature. The black curve is depth/2.

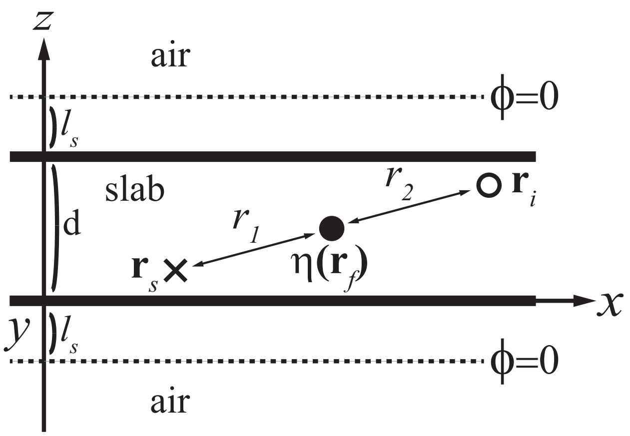

FIG. 2. Model geometry for an infinite slab of thickness d, where $\mathbf{r} = (x, y, z)$ and the y-axis is going into the page. An excitation source (X) at $\mathbf{r}_s$ and a fluorescence emission detector (O) at $\mathbf{r}_i$ are placed one scattering length $l^* = 3D$ away from the slab boundaries as shown. A fluorescence inhomogeneity (●) is at the unknown position $\mathbf{r}_f$. Zero flux ($\phi = 0$) boundary conditions with $l_s = 5.03D$ are used to simulate an infinite slab geometry [23].

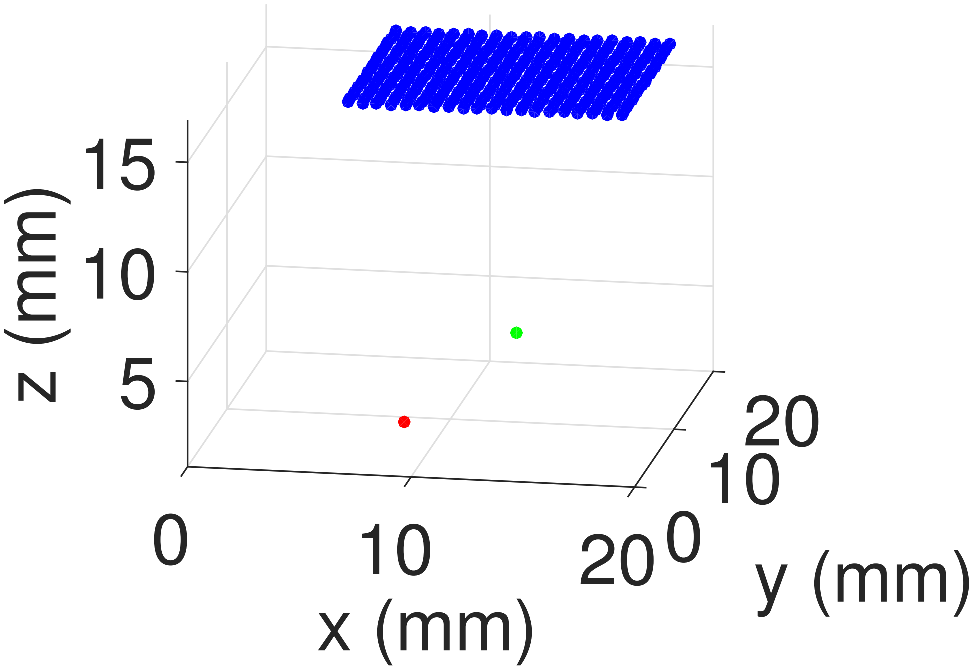

FIG. 3. Slab problem geometry with $\mathbf{r}_s = (8.09, 9.07, 1.11)$ mm plotted as the red point, $\mathbf{r}_{ft} = (12.77, 10.79, 5.0)$ mm plotted as the green point, and $N = 400$ detector locations $\mathbf{r}_i$ plotted as blue points. These positions were used so that the simulation and experimental results can be compared. The slab has the same dimensions (18 mm thick) and properties as used in the experiment.

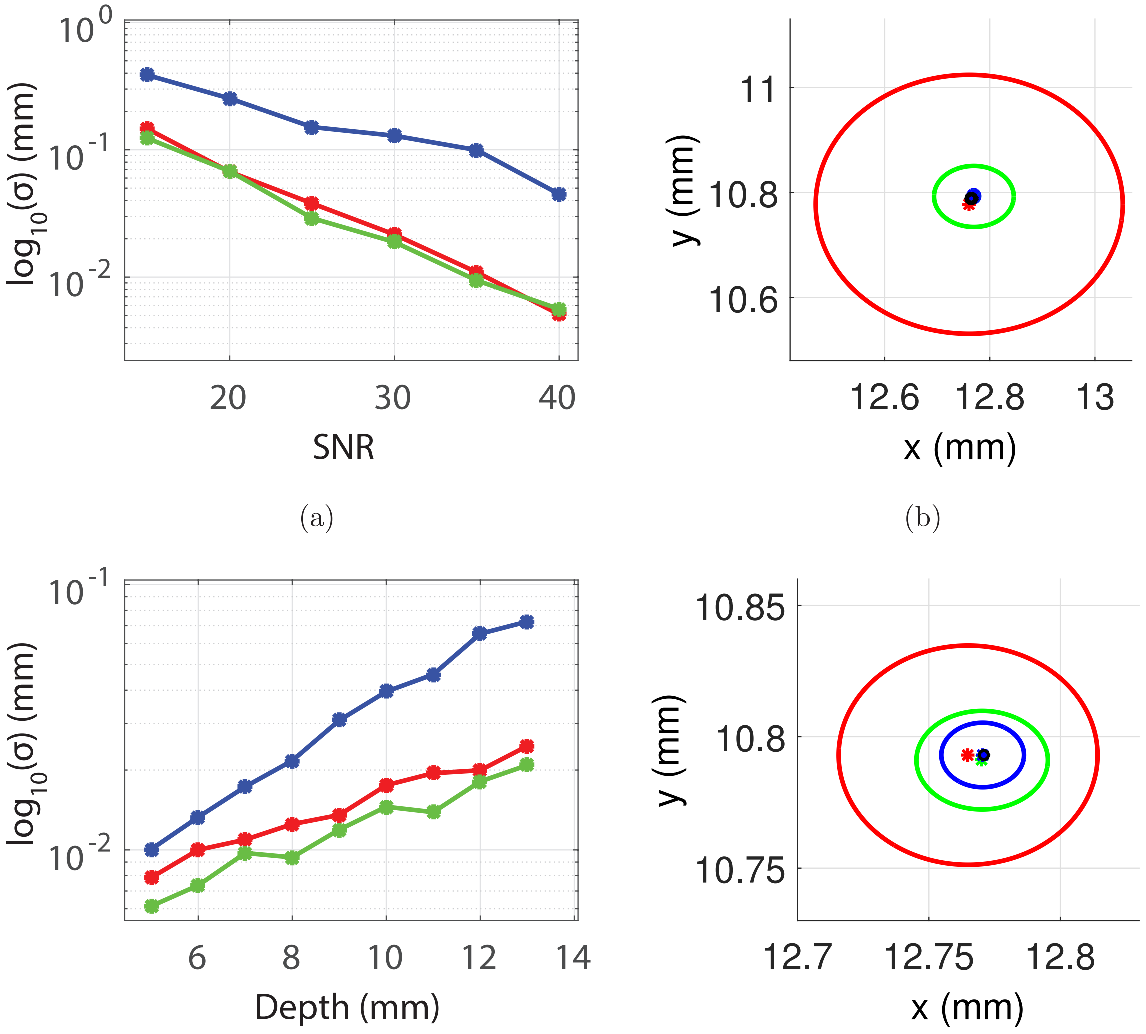

(a) (b)

(c) (d)

FIG. 4. Uncertainty in the numerical localization of a fluorescent inhomogeneity in the slab geometry shown in Fig. 3. The standard deviations were estimated using 50 noisy independent measurements that were generated using (11) and (12). (a) $\hat{\sigma}_x$, $\hat{\sigma}_y$, and $\hat{\sigma}_z$ versus SNR plotted as red, green, and blue curves, respectively. The depth of the fluorescent inhomogeneity was 13 mm, as shown in Fig. 3. $\hat{\sigma}_z$ is larger than $\hat{\sigma}_x$ and $\hat{\sigma}_y$ because the detectors are only in the $x-y$ plane. (b) Ellipses in the $x-y$ plane with major and minor axes of lengths $4\hat{\sigma}_x$ or $4\hat{\sigma}_y$ and means given by their center point. Red, green, and blue ellipses correspond to SNRs of 15 dB, 25 dB, and 40 dB, respectively. (c) $\hat{\sigma}_x$, $\hat{\sigma}_y$, and $\hat{\sigma}_z$ versus depth plotted as red, green, and blue curves, respectively, with 30 dB SNR. (d) Ellipses in the $x-y$ plane with major and minor axes of length $4\hat{\sigma}_x$ or $4\hat{\sigma}_y$ and means given by their center point. Red, green, and blue ellipses correspond to depths of 13 mm, 8 mm, and 5 mm, respectively.

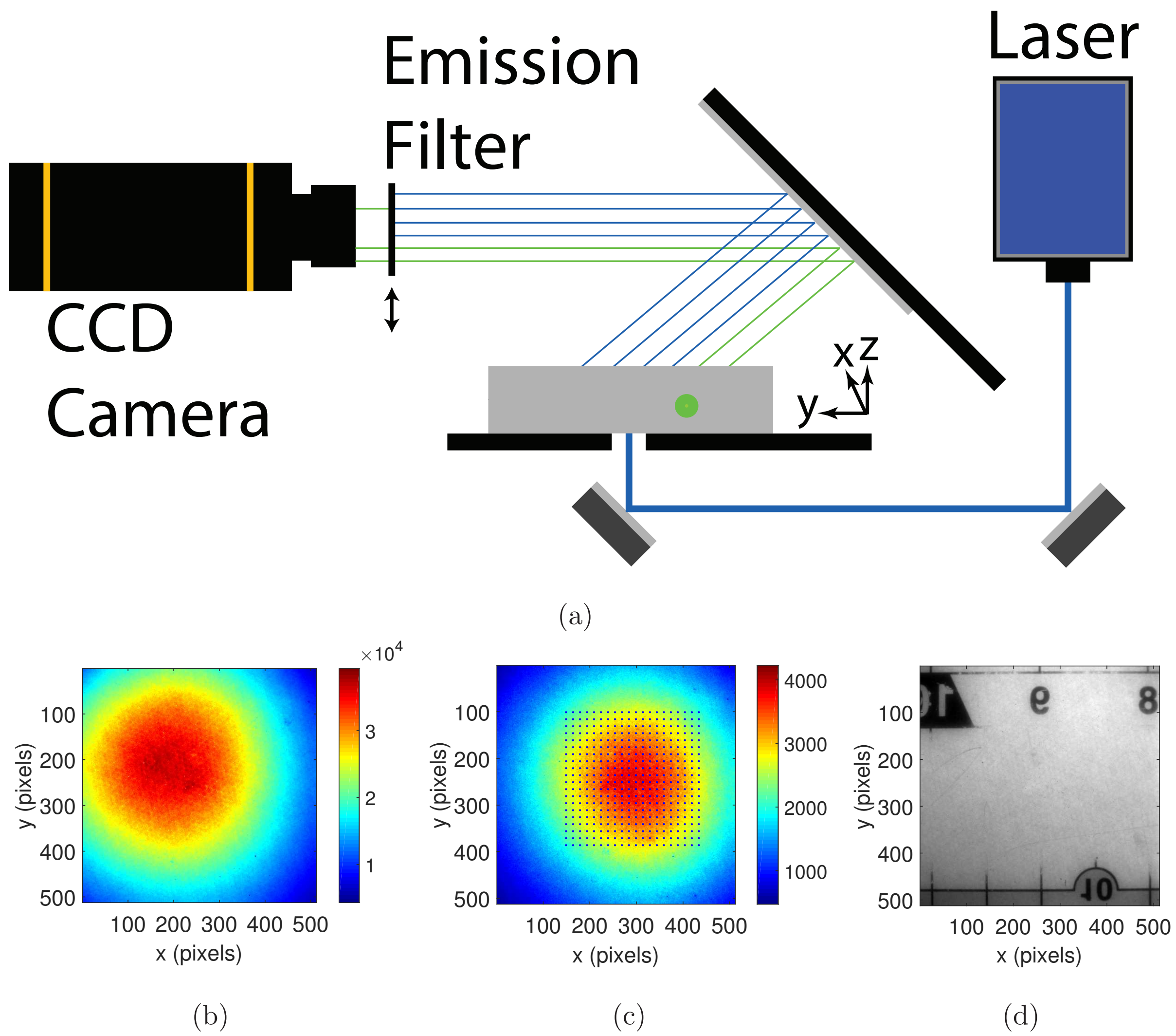

(a)

(b) (c) (d)

FIG. 5. (a) Experiment setup for localization of a fluorescent inhomogeneity (green point). The fluorescent inhomogeneity (ATTO 647N) is embedded in a highly scattering slab that is 18 mm thick. The laser source is a filtered pulsed supercontinuum source (EXR-20 NKT Photonics, 5 ps seed pulse width, 20 MHz repetition rate, VARIA tunable filter). The laser source is tuned to λ_x, and detection is by a CCD camera with or without a bandpass filter at λ_m. (b) Light at λ_x detected by the CCD camera without the bandpass filter. Because the bandpass filter attenuates the excitation light by a factor of 10^6, the fluorescent signal is negligible compared to the transmitted excitation light when the bandpass filter is not used. (c) Light at λ_m (after background subtraction) detected by the CCD camera with the bandpass filter. The positions of the 400 detectors are shown as blue dots. (d) CCD image of a ruler showing the field of view (about 22.02 mm by 22.02 mm). Images of the ruler were used to convert pixels to mm.

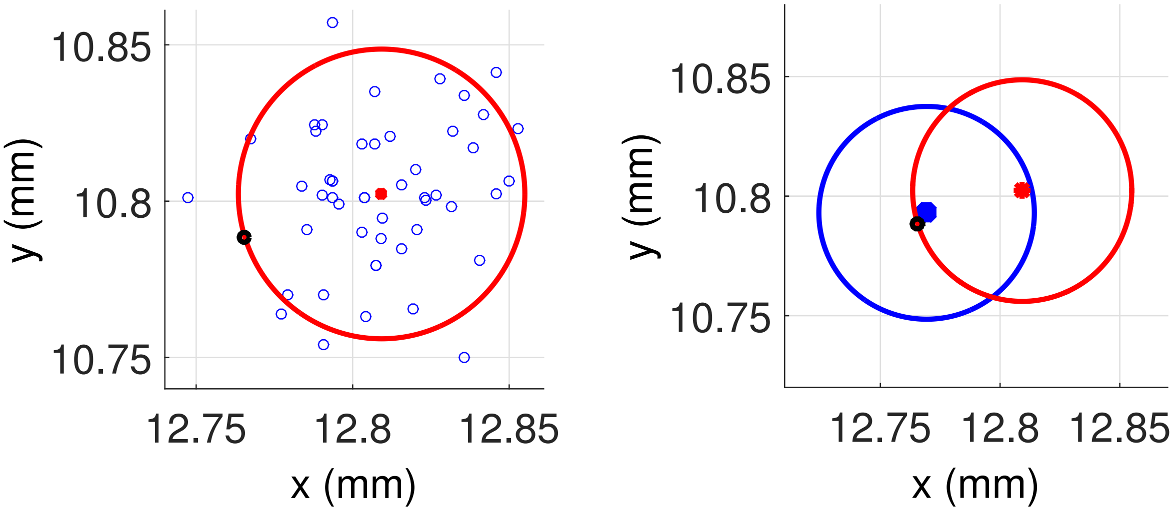

(a)

(b)

FIG. 6. Experimental localization uncertainty for the fluorescent inhomogeneity embedded in the highly scattering slab of Fig. 5. Experimental values for $\hat{\sigma}_x$, $\hat{\sigma}_y$, and $\hat{\sigma}_z$ were estimated using 50 independent experimental measurements. (a) Plot of the (x, y) components of the localized positions as blue points. These points were used to calculate the major and minor axes of the red ellipse, which have dimensions $4\hat{\sigma}_x$ or $4\hat{\sigma}_y$, as well as its center red point, which is the mean. The black point is the true location that was estimated with a 2-D Gaussian fit. (b) Comparison of the experimental uncertainty to the numerical uncertainty. The blue ellipse was generated from numerical data with mean SNR= 28.9 dB to match the experimental value, and the red ellipse is the same as in (a). See Table I for the numerical values.

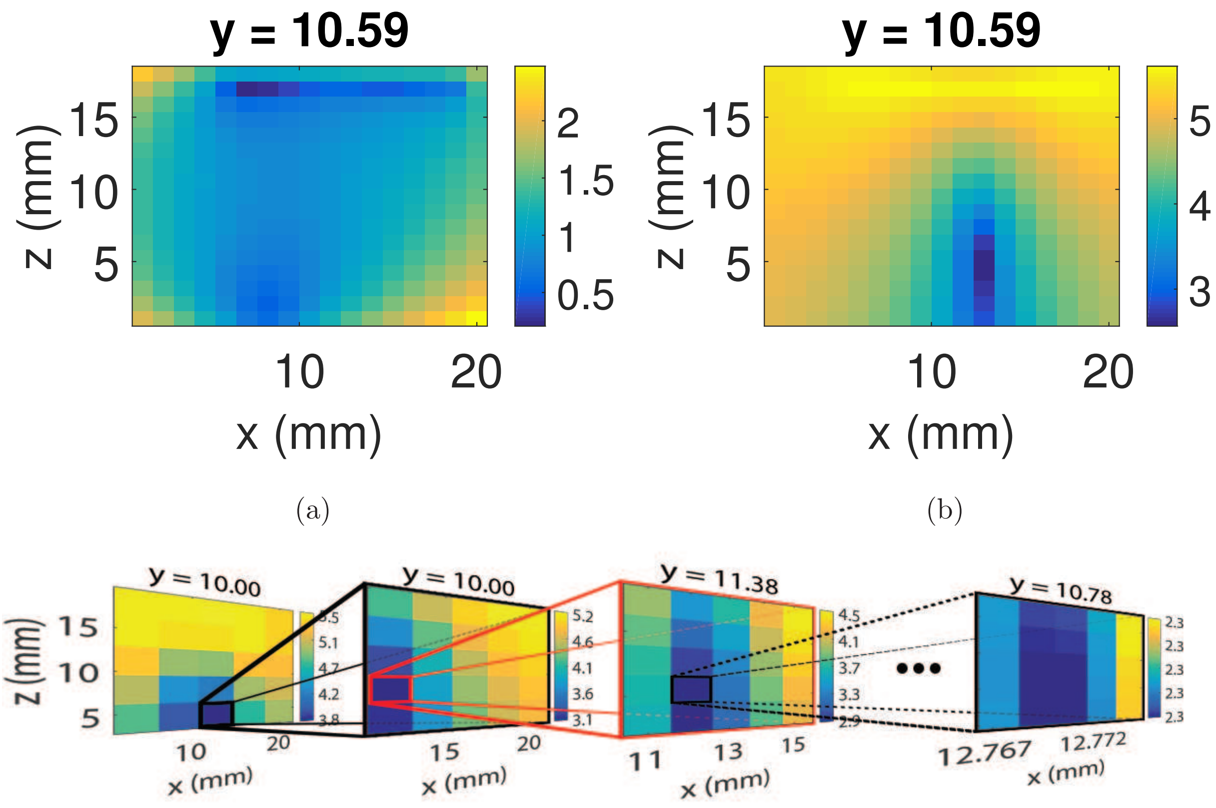

(a)

(b)

(c)

FIG. 7. Numerical localization of a point fluorescent inhomogeneity embedded in a highly scattering slab with the same dimensions and properties as used in the experiment. The slab problem geometry is illustrated in Fig. 3. Measurements were simulated using (4) with $w = 10$ and a 30 dB SNR, and $\tilde{w}(\mathbf{r}_f)$ from (7) and $c(\mathbf{r}_f)$ from (8) were evaluated over the region of interest. (a) Plot of $\tilde{w}(\mathbf{r}_f)$ slice and (b) plot of $c(\mathbf{r}_f)$ slice for fixed y, such that the plots contains the point that minimizes $c(\mathbf{r}_f)$. The values of fixed y are shown above the plots, and the color bars have log scales with arbitrary units. Using (9), $\hat{\mathbf{r}}_f = (12.94, 10.59, 5.29)$, and using (10), $\hat{w} = 10.07$. The localization errors in the x, y, and z dimensions are 1.37%, 1.85%, and 5.88%, respectively. The course discretization of the region of interest is a primary contributor to the estimation error. (c) Localization with multiresolution. Plots of $c(\mathbf{r}_f)$ slices for fixed y are shown for multiresolution iterations 1, 2, 3, and 13. At iteration 13, from (9), $\hat{\mathbf{r}}_f = (12.77, 10.78, 4.98)$, and from (10), $\hat{w} = 10.02$. The localization errors in the x, y, and z dimensions are 0.05%, 0.05%, and 0.19%, respectively. The discretization error has been minimized.

TABLES

TABLE I. Estimated numerical and experimental localization uncertainties, means, and resulting resolution (mm). The resolution of FDOT is assumed to be depth/2.

	SRDOI Numerical	SRDOI Experimental	FDOT
$(\hat{\sigma}_x, \hat{\sigma}_y, \hat{\sigma}_z)$	$(0.0225, 0.0222, 0.1301)$	$(0.0229, 0.0232, 0.1089)$	–
$(\hat{\mu}_x, \hat{\mu}_y, \hat{\mu}_z)$	$(12.769, 10.793, 4.972)$	$(12.809, 10.802, 4.875)$	–
Resolution	$(0.0530, 0.0523, 0.3064)$	$(0.0539, 0.0546, 0.2564)$	6.5